IMA Journal of Applied Mathematics (2021) **86**, 490–501
doi:10.1093/imamat/hxab004
Advance Access publication on 22 April 2021

Longitudinal thermocapillary slip about a dilute periodic mattress of protruding bubbles

Ehud Yariv*
Department of Mathematics, Technion—Israel Institute of Technology, Haifa 32000, Israel
*Corresponding author: udi@technion.ac.il

and

Toby L. Kirk
Mathematical Institute, University of Oxford, Oxford OX2 6GG, UK

[Received on 14 April 2020; revised on 10 November 2020; accepted on 15 February 2021]

A common realization of superhydrophobic surfaces comprises of a periodic array of cylindrical bubbles which are trapped in a periodically grooved solid substrate. We consider the thermocapillary animation of liquid motion by a macroscopic temperature gradient which is longitudinally applied over such a bubble mattress. Assuming a linear variation of the interfacial tension with the temperature, at slope σ_T, we seek the effective velocity slip attained by the liquid at large distances away from the mattress. We focus upon the dilute limit, where the groove width $2c$ is small compared with the array period $2l$. The requisite velocity slip in the applied-gradient direction, determined by a local analysis about a single bubble, is provided by the approximation

$$\pi \frac{G\sigma_T c^2}{\mu l} I(\alpha),$$

wherein G is the applied-gradient magnitude, μ is the liquid viscosity and $I(\alpha)$, a non-monotonic function of the protrusion angle α, is provided by the quadrature,

$$I(\alpha) = \frac{2}{\sin\alpha} \int_0^\infty \frac{\sinh s\alpha}{\cosh s(\pi - \alpha) \sinh s\pi} \, \mathrm{d}s.$$

Keywords: superhydrophobic surfaces; thermocapillary flows; matched asymptotic expansions.

1. Introduction

Superhydrophobic surfaces, originally renowned for their non-wetting properties, have become attractive to the fluid-mechanical community due to their drag reduction promise (Rothstein, 2010). To quantify this drag reduction, it is common to employ a canonical flow problem where the surface is exposed to an otherwise-uniform shear; the associated 'slip length', representing a far-field velocity offset, provides a measure of the surface slipperiness (Crowdy, 2015; Luca *et al.*, 2018). Since superhydrophobic surfaces are generally anisotropic, the slip length is represented by a second-rank symmetric tensor, with two principal directions in the plane of shear.

A common superhydrophobic configuration consists of an infinite array of cylindrical bubbles that are trapped in a periodically grooved solid substrate (Ou & Rothstein, 2005). In that 'bubble mattress'

geometry, the principal directions correspond to the 'longitudinal' and 'transverse' problems, where the shear is respectively applied along and perpendicular to the grooves. A complete specification of the slip-length tensor accordingly requires the solution of these two flow problems. It was observed by Lauga & Stone (2003) that the earliest solution of these problems was carried out by Philip (1972a,b) (in a different physical context) for the case of flat menisci. In that special case, the ratio of the slip length to the array period is a function of a single parameter, the 'gas fraction' of the compound surface.

An alternative to the above 'mechanical' animation entails 'thermal' animation, using a macroscopic temperature gradient which is imposed parallel to the surface. Marangoni forces which act at the menisci generate thermocapillary flow, which approaches a finite 'slip' velocity at large distances away from the surface. This velocity slip constitutes the analog of the slip-length concept in shear-driven flows. The pioneering analysis of thermocapillary flow about a superhydrophobic surface was carried out by Baier *et al.* (2010) who considered the bubble mattress geometry (with flat menisci). Baier *et al.* (2010) made use of the 'standard model' of flows about superhydrophobic surfaces, implicit in Philip (1972a), where both liquid inertia and gas viscosity are neglected. In addressing the thermal problem, moreover, they made use of the prevailing assumptions in the thermocapillary literature (Young *et al.*, 1959), assuming a linear variation of the surface-tension coefficient with the temperature and neglecting the gas conductivity. They additionally assumed a highly conducting solid substrate, such as silicon. With that latter assumption, the solid temperature profile is independent of that in the liquid.

In the longitudinal problem, where the external gradient is applied along the grooves, the temperature field in the solid substrate simply coincides with the macroscopic profile, which varies linearly with the longitudinal coordinate. As a result, the temperature profile in the liquid phase constitutes a superposition of the above linear variation and an excess-temperature field, animated by advection, which is independent of that coordinate. The ensuing flow then varies only in the cross-sectional plane. The above translational invariance results, in turn, in a convenient decoupling, where the longitudinal velocity component is independent of both the excess-temperature field and the accompanying cross-sectional flow. Thus, if interest is limited to that component (as would be the case if one only sought to calculate the effective slip), there is no need to address the (nonlinearly coupled) problem governing the excess-temperature field and cross-sectional flow. Using Lorentz reciprocity, Baier *et al.* (2010) showed that the longitudinal thermocapillary slip is proportional to the slip length in the comparable shear-driven problem, the latter having been calculated by Philip (1972a,b). The longitudinal thermocapillary problem has been discussed further by Yariv (2018) who identified a simple analogy between the longitudinal velocity component and the comparable component in the associated mechanically driven problem.

Both the pioneering analysis of Baier *et al.* (2010) and the followup analysis of Yariv (2018) are restricted to a flat menisci geometry. There is an obvious interest in going beyond that restriction and allowing for a non-zero protrusion angle of the bubbles. This extension was discussed by Yariv & Crowdy (2020), who showed that the linkage between the slip velocity and slip length, identified by Baier *et al.* (2010), does not hold in the general case of non-zero protrusion angle. Similarly, the analogy identified by Yariv (2018) breaks down in that general case.

Yariv & Crowdy (2020) focused upon the singular limit of near-unity gas fraction. Here we consider the diametric limit of small gas fractions. This consideration is motivated by the literature of shear-driven problems, where the effect of protrusion angles was initially addressed in that 'dilute' limit—first in the transverse case (Davis & Lauga, 2009) and soon after in the longitudinal case (Crowdy, 2010, 2016). In the present context of thermocapillary flow, we only address the longitudinal problem. The present contribution accordingly constitutes the thermocapillary counterpart of Crowdy (2010). The difficulties associated with the transverse thermocapillary problem are described in the conclusions section.

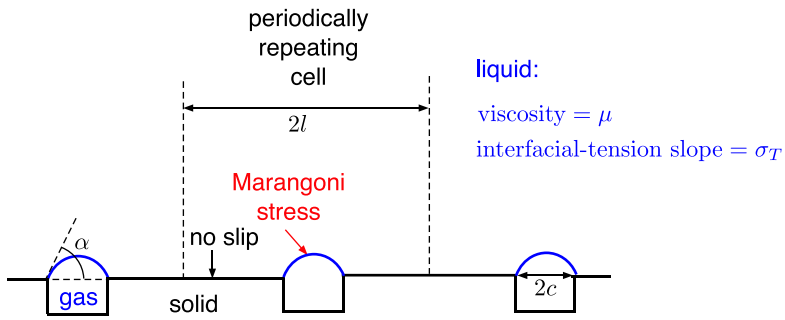

FIG. 1. Schematic of the dimensional geometry.

As in the analysis of Baier *et al.* (2010), we employ the standard model of a flow about bubble mattresses. We accordingly neglect liquid inertia from the outset, represent the bubble menisci as shear-free surfaces and assume the same protrusion angle for all the bubbles. In the context of mechanical animation, each of these approximations has been relaxed to some extent in the recent years. Thus, inertial effects have been addressed by Teo & Khoo (2014); gas-viscosity effects have been discussed by Schönecker *et al.* (2014), Game *et al.* (2017) and Crowdy (2017); and the slow variation in the protrusion angle along the flow has been recently considered by Game *et al.* (2019). In the present thermocapillary context, still at its infancy, we elect to follow Baier *et al.* (2010) in maintaining the simplest possible model.

2. Problem formulation

We consider a bubble-mattress configuration, where a highly conducting flat solid substrate is decorated with a period-$2l$ array of grooves (width $2c$). When immersed in a liquid (viscosity μ), cylindrical bubbles get trapped in the grooves, forming a two-dimensional bubble mattress: see Fig. 1. The protrusion angle of the bubbles is denoted by α. A macroscopic temperature gradient, say of magnitude G, is applied parallel to the grooves. Our interest lies in the thermocapillary flow engendered by the Marangoni forces at the liquid–gas menisci. The flow problem is two dimensional, independent of the coordinate along the grooves. The quantity of interest in the problem is the resulting slip velocity, namely the limiting value attained by that flow at large distances away from surface.

In modeling the thermocapillary transport, we assume a linear variation of the interfacial tension with the temperature, the slope being denoted by σ_T. Using l as a length unit, we employ the Cartesian coordinates (x, y, z) with the z-axis running along the grooves, antiparallel to the applied-gradient direction, the x-axis passing through the solid–liquid interfaces and the y-axis pointing into the liquid. The origin is chosen such that the y-axis bisects one of the bubbles, see Fig. 2. Since the flow is independent of z, we hereafter interpret the gradient operator $\boldsymbol{\nabla}$ as $\hat{\mathbf{e}}_x\,\partial/\partial x + \hat{\mathbf{e}}_y\,\partial/\partial y$. Periodicity allows to consider a single unit cell, say that bounded between the rays $x = \pm 1$. The fluid domain $\mathcal{D}$ in that cell is additionally bounded by the bubble surface $\mathcal{B}$ and the solid boundary $\mathcal{S}$, which consists of the two patches $\Delta < |x| < 1$ at $y = 0$, in which

$$\Delta = c/l \tag{2.1}$$

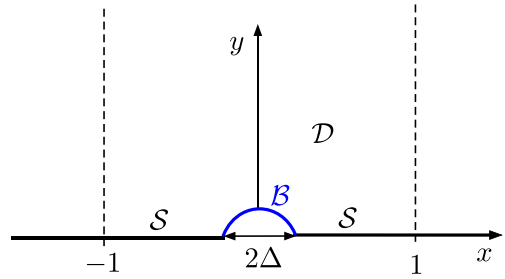

FIG. 2. Schematic of the dimensionless unit cell geometry.

is the gas fraction of the compound surface.

We employ a dimensionless notation where velocities are normalized by $-lG\sigma_T/\mu$ (which is positive in the common case of negative σ_T). The velocity component in the z-direction, say w, satisfies (i) Laplace's equation,

$$\nabla^2 w = 0 \quad \text{in} \quad \mathcal{D}; \tag{2.2}$$

(ii) the Marangoni condition,

$$\hat{\mathbf{n}} \cdot \nabla w = -1 \quad \text{at} \quad \mathcal{B}, \tag{2.3}$$

wherein $\hat{\mathbf{n}}$ is the normal unit vector, pointing into liquid; (iii) the no-slip condition at $\mathcal{S}$,

$$w = 0 \quad \text{at} \quad y = 0 \quad \text{for} \quad \Delta < |x| < 1; \tag{2.4}$$

(iv) the far-field condition

$$\lim_{y\to\infty} \frac{\partial w}{\partial y} = 0, \tag{2.5}$$

representing the absence of imposed shear; and (v) periodicity conditions at $x = \pm 1$. Since w is clearly an even function of x, these conditions may be written

$$\frac{\partial w}{\partial x} = 0 \quad \text{at} \quad x = \pm 1. \tag{2.6}$$

With the exception of the Marangoni condition (2.3), which now applies over a curved meniscus, the preceding formulation coincides with that of Yariv (2018).

Our interest lies in the effective slip velocity

$$w_\infty = \lim_{y\to\infty} w. \tag{2.7}$$

This quantity is a function of the two geometric parameters of the problem, namely the gas fraction Δ and the protrusion angle α, which appears implicitly in condition (2.3). In the case of a flat meniscus,

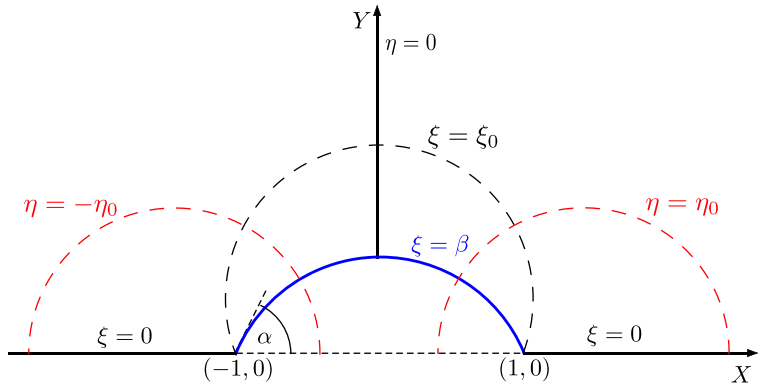

FIG. 3. Dimensionless bubble-scale geometry. Also shown are representative isolines of the bipolar coordinates, $\xi = \xi_0$ and $\eta = \pm\eta_0$, with $0 < \xi_0 < \beta$ and $\eta_0 > 0$.

$\alpha = 0$, w_∞ coincides with the slip length of the corresponding shear problem. (This literal coincidence, as opposed to the mere proportionality originally shown by Baier *et al.*, 2010, is a consequence of the present non-dimensionalization.) The latter has been calculated by Philip (1972a); making use of his result, we accordingly have, for all Δ-values,

$$w_\infty = -\frac{2}{\pi} \ln \cos \frac{\pi \Delta}{2} \quad \text{for} \quad \alpha = 0. \tag{2.8}$$

3. The dilute limit

As explained in the Introduction, exact solutions are presently available only in the flat-meniscus case $\alpha = 0$. In what follows, we consider the dilute limit, $\Delta \ll 1$, which allows to derive approximate solutions for arbitrary α. We employ matched asymptotic expansions, separately analyzing the flow on the scale of the period and on the scale of the bubble. The latter is resolved using the stretched coordinates

$$X = x/\Delta, \quad Y = y/\Delta, \tag{3.1}$$

corresponding to length normalization by c; the associated stretched position vector $X\hat{\mathbf{e}}_x + Y\hat{\mathbf{e}}_y$ is denoted by $\mathbf{X}$, while the associated gradient operator $\hat{\mathbf{e}}_x\, \partial/\partial X + \hat{\mathbf{e}}_y\, \partial/\partial Y$ is denoted by $\boldsymbol{\nabla}_{\mathbf{X}}$. Boundary conditions on $\mathcal{B}$ now apply in the bubble-scale problem, while the far-field and periodicity conditions (2.5) and (2.6) apply in the period-scale problem. It is evident that the bubble-scale region is unbounded in the X-coordinate, see Fig. 3.

It is useful to reformulate the flow problem in the bubble-scale region. With condition (2.3) suggesting that w is $O(\Delta)$ we write

$$w = \Delta W \tag{3.2}$$

where W is an $O(1)$ function of X and Y. An even function of X, it satisfies Laplace's equation in the stretched coordinates, $\nabla^2_{\mathbf{X}} W = 0$. In terms of these coordinates, condition (2.3) becomes

$$\hat{\mathbf{n}} \cdot \nabla_{\mathbf{X}} W = -1 \quad \text{at} \quad \mathcal{B}, \tag{3.3}$$

while condition (2.4) gives, at leading order,

$$W = 0 \quad \text{for} \quad |X| > 1 \quad \text{at} \quad Y = 0. \tag{3.4}$$

In what follows, we make use of bipolar coordinates (see Fig. 3), defined via the relations (Happel & Brenner, 1965)

$$X = \frac{\sinh \eta}{\cosh \eta - \cos \xi}, \quad Y = \frac{\sin \xi}{\cosh \eta - \cos \xi}. \tag{3.5}$$

The constant-η curves constitute a family of non-intersecting circles of radius $1/|\sinh \eta|$, centered about $(\coth \eta, 0)$; in particular, $\eta = 0$ on the Y-axis. In the upper-XY-plane, the constant-ξ curves constitute a family of circular arcs of radius $1/\sin \xi$, all passing through the limiting points $(\pm 1, 0)$. In terms of these coordinates, $\mathcal{S}$ coincides with $\xi = 0$ while the interface $\mathcal{B}$ coincides with $\xi = \pi - \alpha \stackrel{\text{def}}{=} \beta$; the fluid domain is $-\infty < \eta < \infty, 0 < \xi < \beta$. The infinity in the upper XY-plane corresponds to $\xi, \eta \to 0$. In that limit, it follows from (3.5) that

$$X \sim \frac{2\eta}{\xi^2 + \eta^2}, \quad Y \sim \frac{2\xi}{\xi^2 + \eta^2}, \tag{3.6}$$

whereby

$$R^2 \sim \frac{4}{\xi^2 + \eta^2} \tag{3.7}$$

in which $R = \sqrt{X^2 + Y^2}$.

In terms of the bipolar coordinates, the gradient and Laplacian operators adopt the respective forms,

$$\nabla_{\mathbf{X}} = \frac{1}{h}\left(\hat{\mathbf{e}}_\xi \frac{\partial}{\partial \xi} + \hat{\mathbf{e}}_\eta \frac{\partial}{\partial \eta}\right), \quad \nabla^2_{\mathbf{X}} = \frac{1}{h^2}\left(\frac{\partial^2}{\partial \xi^2} + \frac{\partial^2}{\partial \eta^2}\right), \tag{3.8}$$

wherein

$$h = \frac{1}{\cosh \eta - \cos \xi} \tag{3.9}$$

is the metric coefficients of both ξ and η.

4. Analysis

We begin with the analysis of the 'inner' bubble-scale problem. Rewriting the problem governing W in bipolar coordinates, we have Laplace's equation,

$$\frac{\partial^2 W}{\partial \xi^2} + \frac{\partial^2 W}{\partial \eta^2} = 0, \tag{4.1}$$

together with the Neumann condition [cf. (3.3)]

$$\frac{1}{h}\frac{\partial W}{\partial \xi} = 1 \quad \text{at} \quad \xi = \beta \tag{4.2}$$

and the Dirichlet condition [cf. (3.4)]

$$W = 0 \quad \text{at} \quad \xi = 0. \tag{4.3}$$

Clearly, W is an even function of η.

It follows from (4.1) that the eigenfunctions of Laplace's equation in bipolar coordinates have the familiar structure of those in Cartesian coordinates. Thus, the most general even function of η which satisfies Laplace's equation and the homogeneous condition (4.3) and does not diverge at infinity is

$$W = \int_0^\infty A(s) \sinh s\xi \cos s\eta \, \mathrm{d}s, \tag{4.4}$$

where, in view of condition (4.2), $A(s)$ also depends upon the parameter β (or α). Defining

$$I = \int_0^\infty sA(s) \, \mathrm{d}s \tag{4.5}$$

(a function of α), we note that $W \sim \xi I$ for $\xi^2 + \eta^2 \to 0$. Making use of (3.6) and (3.7), we conclude that

$$W \sim \frac{2I(\alpha)Y}{R^2} \quad \text{for} \quad R \to \infty, \tag{4.6}$$

representing a two-dimensional dipole which is oriented in the y-direction.

The function $A(s)$ is determined from the inhomogeneous condition (4.2), which gives

$$\frac{1}{\cosh \eta - \cos \beta} = \int_0^\infty sA(s) \cosh s\beta \cos s\eta \, \mathrm{d}s. \tag{4.7}$$

Upon using the transform (Davis & Lauga, 2009)

$$\frac{1}{\cosh \eta + \cos \alpha} = \frac{2}{\sin \alpha} \int_0^\infty \frac{\sinh s\alpha}{\sinh s\pi} \cos s\eta \, \mathrm{d}s \tag{4.8}$$

we find that

$$sA(s) = \frac{2\sinh s\alpha}{\sin\alpha\cosh s(\pi-\alpha)\sinh s\pi}. \tag{4.9}$$

Consider now the 'outer' period-scale problem. At leading-order, the fluid domain $\mathcal{D}$ becomes a semi-strip, namely $y > 0$ with $-1 < x < 1$, while the interface $\mathcal{B}$ shrinks to a singular point at the origin. In view of the scaling (3.1) and (3.2) together with the $1/R$ decay rate in (4.6), it is evident that w is $O(\Delta^2)$ in that region. This suggests there the rescaling

$$w = \Delta^2\tilde{w}, \tag{4.10}$$

with $\tilde{w}$ being an $O(1)$ function of x and y. The function $\tilde{w}$ is governed by (i) Laplace's equation [cf. (2.2)],

$$\nabla^2\tilde{w} = 0 \quad \text{for} \quad y > 0 \quad (-1 < x < 1); \tag{4.11}$$

(ii) the no-slip condition [cf. (2.4)],

$$\tilde{w} = 0 \quad \text{at} \quad y = 0 \quad \text{for} \quad 0 < |x| < 1; \tag{4.12}$$

(iii) the far-field condition [cf. (2.5)],

$$\lim_{y\to\infty}\frac{\partial\tilde{w}}{\partial y} = 0; \tag{4.13}$$

and (iv) the periodicity condition [cf. (2.6)],

$$\frac{\partial\tilde{w}}{\partial x} = 0 \quad \text{at} \quad x = \pm 1. \tag{4.14}$$

The Marangoni condition (2.3) does not apply at the period scale; instead, one needs to impose asymptotic matching with the bubble-scale solution. Making use of (4.6) and (4.10), this gives the following:

$$\tilde{w} \sim \frac{2I(\alpha)y}{x^2+y^2} \quad \text{as} \quad x^2+y^2 \to 0. \tag{4.15}$$

Since conditions (4.12)–(4.14) are all homogeneous, it is condition (4.15) that triggers the period-scale flow.

It is not difficult to see that the solution to the preceding problem is given by the infinite sum

$$\tilde{w} = 2I(\alpha)y\sum_{n=-\infty}^{\infty}\frac{1}{(x-2n)^2+y^2}, \tag{4.16}$$

which represents an infinite collection of dipoles situated at the singular points corresponding to the bubbles. The series appearing in (4.16) has a convenient complex representation, which follows from the Mittag–Leffler expansion of the cotangent. We accordingly obtain

$$\tilde{w} = -\pi I(\alpha)\,\mathrm{Im}\left\{\cot\frac{\pi z}{2}\right\}, \quad z = x + iy. \tag{4.17}$$

Since $\cot(\pi z/2) \to -i$ at large y, we find that

$$\lim_{y\to\infty} \tilde{w} = \pi I(\alpha). \tag{4.18}$$

The above analysis should be contrasted with the approach of Davis & Lauga (2009), where a sum similar to that appearing in (4.16) was evaluated at large y using an averaging procedure.

5. Effective slip

It follows from definition (2.7) and result (4.18) that

$$w_\infty \sim \Delta^2 \pi I(\alpha) \quad \text{for} \quad \Delta \ll 1. \tag{5.1}$$

The function $I(\alpha)$ is calculated by substituting (4.9) into (4.5), giving the expression which appears in the abstract. For $\alpha = 0$, quadrature gives $I = 1/4$. The resulting leading-order approximation, $w_\infty/\Delta^2 = \pi/4 \approx 0.7854$, agrees with the small-$\Delta$ limit of (2.8). For $\alpha = \pi/2$, we find $w_\infty/\Delta^2 = 2$, while for $\alpha = -\pi/2$ we find $w_\infty/\Delta^2 = 2(4\pi\sqrt{3} - 9)/27 \approx 0.9456$.

The non-monotonic dependence implied by the above figures is indeed observed in Fig. 4, where the variation with α of w_∞/Δ^2, as obtained from (4.5) and (5.1), is portrayed. The maximum slip velocity is attained at $\alpha = \pi/2$, while the minimum velocity is attained at $\alpha = -\pi/6$, where $w_\infty/\Delta^2 \approx 0.7427$. The monotonic increase of w_∞ at positive values of α is reminiscent to the increase of the longitudinal slip length with α at the shear-driven problem (Crowdy, 2010).

The Δ^2 scaling of the velocity slip (5.1) may be traced back to the Δ scaling of the bubble-scale velocity, itself a consequence of the Marangoni condition. The additional Δ factor results from the $1/R$-type velocity decay [see (4.6)]. The dimensional slip expression corresponding to (5.1) is provided in the abstract; it is proportional to c^2, a feature which is also exhibited in the comparable shear-driven problems (Crowdy, 2010; Davis & Lauga, 2009). In these problems, the Δ scaling of the bubble-scale velocity stems from the $O(\Delta)$ magnitude of the driving shear flow at the bubble region.

The transition from an $O(\Delta)$ velocity field on the bubble scale to an $O(\Delta^2)$ velocity field on the period scale is evident from the following composite asymptotic solution of the longitudinal velocity component (cf. Crowdy, 2016)

$$\Delta W + \Delta^2\tilde{w} - \Delta^2\frac{2I(\alpha)y}{x^2+y^2} = \Delta W - \Delta^2\pi I(\alpha)\,\mathrm{Im}\left\{\cot\frac{\pi z}{2} - \frac{2}{\pi z}\right\}, \tag{5.2}$$

which provides a uniform approximation for w in $\mathcal{D}$.

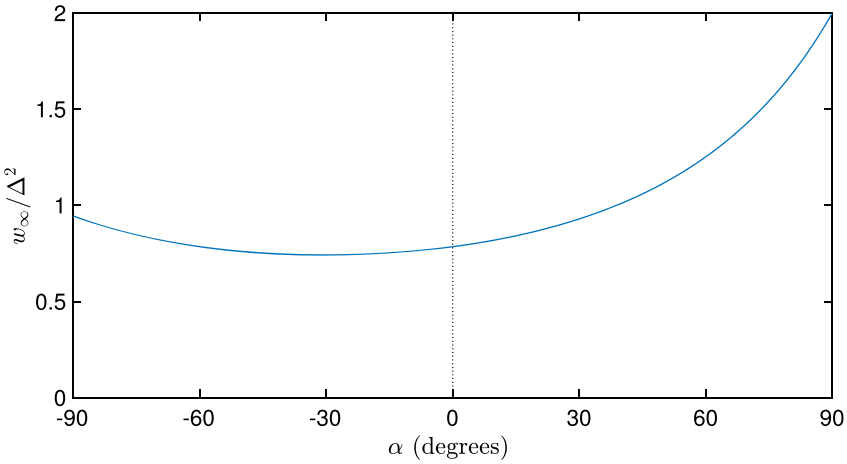

FIG. 4. Dependence upon α of the leading-order slip velocity, as determined from (4.5), (4.9) and (5.1).

6. Concluding remarks

Assuming a highly conducting solid substrate, we have calculated the longitudinal thermocapillary slip over a dilute bubble mattress. We found a non-monotonic dependence of the slip upon the protrusion angle α, with a minimum at $\alpha = -30°$. The slip is positive for the entire range $(-90°, 90°)$ of protrusion angle. The problem exhibits a clear asymmetry between convex and concave bubbles.

In obtaining approximation (5.1), we have made use of matched asymptotic expansions, with separate expansions in two regions, one in the vicinity of a representative bubble and one away from the bubbles. In principle, one could adopt a less formal approach, as in Davis & Lauga (2009) and Crowdy (2010). The latter approach has a weakness—the solution scheme may appear contradictory, in the sense that a non-zero far-field slip is obtained from a collection of single-bubble solutions, each required to satisfy a far-field decay. (A similar apparent self-contradiction may appear to be present in the analysis of Davis & Lauga, 2009, and Crowdy, 2010, if one considers the perturbation relative to the imposed shear.) In the formal approach used herein, it is readily observed that the above-mentioned fields belong to different asymptotic regions and are of different asymptotic orders.

In principle, one could have obtained the velocity slip using reciprocity relations—an approach which has been used extensively in mechanically driven problems (Kirk *et al.*, 2020; Crowdy, 2017a,b, 2016). Indeed, it was shown in Appendix A of Yariv & Crowdy (2020) that the slip velocity may be expressed as a single quadrature which involves the velocity distribution in the comparable shear-driven problem. In the dilute limit, this distribution is provided in Crowdy's papers (Crowdy, 2010, 2016). We have preferred to employ a direct asymptotic approach, which has the benefit of revealing the flow field that underlies the velocity slip.

The key to the simplification of the longitudinal problem considered herein is the coincidence, identified by Baier *et al.* (2010), of the solid-phase temperature with the macroscopic profile. This coincidence, in turn, results in the simple boundary-value problem governing the longitudinal velocity component that was posed in Section 2. No such simplification arises in the transverse problem, where the solid temperature profile has to be solved for. It was noted by Baier *et al.* (2010) that when the solid slats that separate the grooves are long, the temperature at their ends is approximately uniform. Making use of that approximation and assuming zero protrusion angle, Yariv & Crowdy (2019) showed that

the harmonic conjugate of that field is related to the 'longitudinal' velocity component in a comparable shear-driven problem about an interchanged boundary—a quantity which was calculated in detail by Philip (1972a). Making use of Lorentz reciprocity, Yariv & Crowdy (2019) reduced the calculation of the velocity slip to the evaluation of a simple quadrature, which depends only upon the gas fraction.

Upon making use of the long-slat approximation, it is possible to analyze the transverse problem in the dilute limit for arbitrary protrusion angles. It is doubtful, however, whether such an analysis is related to a realistic problem. The long-slat approximation is expected to hold provided the length of the slats is large compared to the period l. Since the former is comparable to the groove width in common configurations (Tsai *et al.*, 2009; Bolognesi *et al.*, 2014), the long-slat approximation is practically incompatible with the dilute limit.

Funding

Israel Science Foundation (1081/16 to E.Y.).

References

Baier, T., Steffes, C. & Hardt, S. (2010) Thermocapillary flow on superhydrophobic surfaces. *Phys. Rev. E*, **82**, 037301.

Bolognesi, G., Cottin-Bizonne, C. & Pirat, C. (2014) Evidence of slippage breakdown for a superhydrophobic microchannel. *Phys. Fluids*, **26**, 082004–12.

Crowdy, D. (2010) Slip length for longitudinal shear flow over a dilute periodic mattress of protruding bubbles. *Phys. Fluids*, **22**, 121703.

Crowdy, D. (2015) A transform method for Laplace's equation in multiply connected circular domains. *IMA J. Appl. Math.*, **80**, 1902–1931.

Crowdy, D. (2017a) Effect of shear thinning on superhydrophobic slip: Perturbative corrections to the effective slip length. *Phys. Rev. Fluids*, **2**, 124201.

Crowdy, D. G. (2016) Analytical formulae for longitudinal slip lengths over unidirectional superhydrophobic surfaces with curved menisci. *J. Fluid Mech.*, **791**, R7–12.

Crowdy, D. G. (2017b) Perturbation analysis of subphase gas and meniscus curvature e.ects for longitudinal flows over superhydrophobic surfaces. *J. Fluid Mech.*, **822**, 307–326.

Davis, A. M. J. & Lauga, E. (2009) Geometric transition in friction for flow over a bubble mattress. *Phys. Fluids*, **21**, 011701.

Game, S. E., Hodes, M., Keaveny, E. E. & Papageorgiou, D. T. (2017) Physical mechanisms relevant to flow resistance in textured microchannels. *Phys. Rev. Fluids*, **2**, 094102–23.

Game, S. E., Hodes, M. & Papageorgiou, D. T. (2019) Effects of slowly varying meniscus curvature on internal flows in the Cassie state. *J. Fluid Mech.*, **872**, 272–307.

Happel, J. & Brenner, H. (1965) *Low Reynolds Number Hydrodynamics*. Englewood Cliffs, NJ: Prentice-Hall.

Kirk, T. L., Karamanis, G., Crowdy, D. G. & Hodes, M. (2020) *J. Fluid Mech.*, 894.

Lauga, E. & Stone, H. A. (2003) Effective slip in pressure-driven Stokes flow. *J. Fluid Mech*, **489**, 55–77.

Luca, E., Marshall, J. & Karamanis, G. (2018) Longitudinal shear flow over a bubble mattress with curved menisci: arbitrary protrusion angle and solid fraction. *IMA J. Appl. Math.*, **3**, 685–25.

Ou, J. & Rothstein, J. P. (2005) Direct velocity measurements of the flow past drag-reducing ultrahydrophobic surfaces. *Phys. Fluids*, **17**, 103606–11.

Philip, J. R. & Angew, Z. (1972a) Flows satisfying mixed no-slip and no-shear conditions. *Z. Angew. Math. Phys.*, **23**, 353–372.

Philip, J. R. & Angew, Z. (1972b) Integral properties of flows satisfying mixed no-slip and no-shear conditions. *Z. Angew. Math. Phys.*, **23**, 960–968.

ROTHSTEIN, J. P. (2010) Slip on superhydrophobic surfaces. *Annu. Rev. Fluid Mech.*, **42**, 89–109.

SCHÖNECKER, C., BAIER, T. & HARDT, S. (2014) Influence of the enclosed fluid on the flow over a microstructured surface in the Cassie state. *J. Fluid Mech.*, **740**, 168–195.

TEO, C. J. & KHOO, B. C. (2014) Effects of interface curvature on poiseuille flow through microchannels and microtubes containing superhydrophobic surfaces with transverse grooves and ribs. *Microfluid. Nanofluid.*, **17**, 891–905.

TSAI, P., PETERS, A. M., PIRAT, C., WESSLING, M., LAMMERTINK, R. G. H. & LOHSE, D. (2009) Quantifying effective slip length over micropatterned hydrophobic surfaces. *Phys. Fluids*, **21**, 112002.

YARIV, E. (2018) Thermocapillary flow between longitudinally grooved superhydrophobic surfaces. *J. Fluid Mech.*, **855**, 574–594.

YARIV, E. & CROWDY, D. (2019) Thermocapillary flow between grooved superhydrophobic surfaces: Transverse temperature gradients. *J. Fluid Mech.*, **871**, 775–798.

YARIV, E. & CROWDY, D. (2020) *SIAM J. Appl. Math*, **80**, 1.

YOUNG, N. O., GOLDSTEIN, J. S. & BLOCK, M. J. (1959) The motion of bubbles in a vertical temperature gradient. *J. Fluid Mech.*, **6**, 350–356.